Deformation lines in Arctic sea ice: intersection angles distribution and mechanical properties

Damien Ringeisen[1,2,3,*], Nils Hutter[4,1,*], and Luisa von Albedyll[1]

[1]Alfred-Wegener-Institut, Helmholtz-Zentrum für Polar- und Meeresforschung, Bremerhaven, Germany
[2]MARUM – Center for Marine Environmental Sciences, Leobener Str. 8, 28359, Bremen, Germany
[3]Department of Atmospheric and Oceanic Sciences, McGill University, Montréal, QC, Canada
[4]Cooperative Institute for Climate, Ocean, and Ecosystem Studies (CICOES), University of Washington, Seattle, WA, United States
[*]These authors contributed equally to this work.

Correspondence: Damien Ringeisen (damien.ringeisen@mcgill.ca) and Nils Hutter (nhutter@uw.edu)

Abstract. ~~In Arctic sea ice, the intersection angles between~~ Despite its relevance for the Arctic climate and ecosystem, modeling sea ice deformation, i.e. the opening, shearing, and ridging of sea ice, along Linear Kinematic Features (LKFs)~~are linked to~~, remains challenging because the mechanical properties of sea ice are not fully understood yet. The intersection angles between LKFs provide valuable information on the internal mechanical properties~~. Sea~~, because they are linked to them. Currently, the LKFs emerging from sea ice rheological models ~~struggle to reproduce the intersection angles between LKFs in Arctic sea ice~~do not reproduce the observed LKFs intersection angles, pointing to a gap in the model physics. We aim to obtain an intersection angle distribution (IAD) from observational data to serve as a reference for high-resolution sea ice models and to infer the mechanical properties of the sea ice cover. We use the sea ice vorticity to discriminate between acute and obtuse LKFs intersection angles within two sea ice deformation datasets: the RGPS and a new dataset from the MOSAiC drift experiment. Acute angles dominate the IAD, with single peaks at $48° \pm 2$ and $45° \pm 7$. The IAD agrees well between both datasets, despite the difference in scale, time periods, and geographical location. The divergence and shear rates of the LKFs also have the same distribution. The dilatancy angle (the ratio of shear and divergence) is not correlated with the intersection angle. Using the IAD, we infer two important mechanical properties of the sea ice: We found an internal angle of friction in sea ice of $\mu_I = 0.66 \pm 0.02$ and $\mu_I = 0.75 \pm 0.05$. The shape of the yield curve or the plastic potential derived from the observed IAD resembles the teardrop or a Mohr–Coulomb shape. With those new insights, sea ice rheologies used in models can be adapted or re-designed to improve the representation of sea-ice ~~dynamics~~deformation.

1 Introduction

Sea ice deformation is a crucial process for the polar climate. It creates areas of open water that allow enhanced heat and gas exchange, and forms ridges that serve as a habitat for biota and provide barriers to winds and ocean currents. The deformation patterns of sea ice in the Arctic Ocean are dominated by narrow lines where deformation concentrates (Schall and van Hecke, 2010)~~,~~. These lines are known as Linear Kinematic Features (LKFs), failure lines or shear bands (Kwok, 2001). LKFs play

a primary role in the mass and energy budget of the Arctic ocean. First, the creation of thicker ice (ridges) or open water (leads), where sea ice growth is enhanced in winter, takes place along LKFs (Stern et al., 1995; Hopkins, 1994; von Albedyll et al., 2020, 2022). Second, shear motion and ~~brine injection from~~ sea-ice growth along LKFs influence the halocline through

25 pycnocline upwelling and brine injection, respectively (McPhee et al., 2005; Itkin et al., 2015; Nguyen et al., 2012). Finally, open leads govern the polar ocean-atmosphere heat and moisture exchange despite their small total area (Maykut, 1978; Untersteiner, 1961; Tetzlaff et al., 2015). Thus, LKFs are an essential component of the Arctic climate system and need to be accurately represented in regional models for reliable regional weather predictions, navigation charts, and services to Arctic communities.

30 LKFs emerge from the mechanical properties of sea ice. Sea ice is often described as a granular material ~~(Overland et al., 1998; Tremblay~~ (Overland et al., 1998; Tremblay and Mysak, 1997; Feltham, 2005), which exhibits brittle properties (Schulson, 2002; Dansereau et al., 2016). Important mechanical properties of sea ice are imprinted in the orientation of the failure lines relative to the stress direction: Two mechanical parameters are known to play a role in the orientation of the failure lines relative to the stress direction in granular materials (Vermeer, 1990): (1) the material's strength threshold to internal stress leading to deforma-

35 tion, especially the ratio of shear strength to compression strength, named the internal angle of friction (Coulomb, 1773), and (2) the dilatancy, or motion perpendicular to the slip line ~~(Roscoe, 1970). The~~ under which the ice undergoes plastic deformation.(Roscoe, 1970). While the sea ice motion of (2) can be observed via ~~remote sensing. Still~~ satellite remote sensing, the internal stress magnitude and direction of (1) cannot be observed at the Arctic scale~~, such that~~ . Therefore it is impossible to measure the orientation of the LKFs with respect to the stress direction ~~. Instead, we use~~ directly. To overcome those

40 shortcomings and still retrieve the mechanical properties from the orientation of the failure lines, the vorticity at the intersections of LKFs can be used instead. By describing the rotation of ice during deformation, vorticity can be utilized to infer the main stress direction and eventually link it to the intersection angles of the LKFs (Hutter et al., 2022b).

~~Former studies~~ Previous studies on LKF intersection angles report single intersection angles based on small sample sizes across large spatial scales (100m-100km), for example, $28°$ (Marko and Thomson, 1977), $30 \pm 4°$ (Erlingsson, 1988), $30°$

45 (Walter and Overland, 1993), and $34°$ to $36°$ (Cunningham et al., 1994). From the RADARSAT Geophysical Processor System (RGPS) sea ice motion dataset (Kwok et al., 1998), sea ice deformation data were obtained over the Arctic Ocean with a period of 3 days, allowing the automated extraction of LKFs locations and angles (Hutter et al., 2019a; Linow and Dierking, 2017). Recent work based on an LKFs tracking algorithm ~~report~~ reports an intersection angles distribution (IAD) between $0°$ and $90°$ with a peak between $40°$ to $50°$ (Hutter and Losch, 2020). Multi-scale directional analysis ~~(MDA)~~ on the RGPS dataset

50 also shows that small intersection angles are dominant (Mohammadi-Aragh et al., 2020).

None of the current sea ice models can reproduce the observed distribution of LKF intersection angles ~~(Hutter et al., 2022a) . This~~ (Hutter et al., 2022b). LKFs in sea ice models emerge from the rheological model, especially from the threshold of sea ice mechanical properties. This threshold creates LKFs because it includes a change of mechanical properties between large deformations, in the LKFs, and small deformations, in between the LKFs, i.e., viscosity maximum for VP models

55 (Hutchings et al., 2005) and damage for brittle models (Dansereau et al., 2016). This hints that the current implementations of sea ice rheological models are not accurate enough to describe the mechanical properties of sea ice. Most climate models today

simulate sea ice as Viscous-Plastic (VP) medium with an elliptical yield curve and normal flow rule ~~(Hibler, 1979; Stroeve et al., 2014)~~ (Hibler, 1979; Stroeve et al., 2014; Keen et al., 2021). Diffuse small deformations are represented by viscous behavior, while the large deformations along LKFs are represented by plastic behavior (Hutchings et al., 2005). High-resolution sea-ice VP

60   models can represent LKFs at scales 5-7 times larger than their horizontal grid spacing ~~(Hutter et al., 2018; Bouchat et al., 2022; Hutter et al~~ (Hutter et al., 2018; Bouchat et al., 2022; Hutter et al., 2022b). The intersection angle of LKFs depends in the VP rheology framework on parameters that define the constitutive equation: the yield curve that defines the stress at failure and the plastic potential that defines the post-failure deformation called the flow rule (Ringeisen et al., 2021, 2019). ~~Based on their observations of LKFs intersection angles ,~~ Thus, observations of intersection angles of LKFs can be used to constrain those parameters. Er-

65   lingsson (1991) proposed an internal angle of friction of ~~$phi = 15° \pm 2°$~~ $\phi = 15° \pm 2°$ based on their observations of LKFs intersection angles, while Marko and Thomson (1977) proposed $\phi \simeq 62°$. Using a small set of LKF intersecting angles and the assumption that the major principal direction of the sea ice internal stress is perpendicular to the wind direction, Wang (2007) proposed the *curved diamond* yield curve. However, there seems to be a need for improvement. LKFs-tracking algorithms show that the current VP models overestimate the intersection angles, with an IAD peaking at 90°(Hutter et al., 2019a;

70   Hutter and Losch, 2020). This behavior is shared by all other rheological models as a recent comparison of state-of-the-art models revealed ~~(Hutter et al., 2022a)~~(Hutter et al., 2022b), and is also observed using ~~MDA~~ multi-scale directional analysis (Mohammadi-Aragh et al., 2020). To improve the IAD in high-resolution sea ice models, the ~~observed~~ presented IAD could be used to improve the definition of weakly constrained sea ice rheological parameters: the yield curve and the plastic potential.

   Studying the intersection angles can provide important insights into two key questions: First, is there a relationship between

75   intersection angles and the divergence (opening or ridging) along the LKF? In other words, does the hypothesis of the normal flow rule (Ringeisen et al., 2019, 2021), as it is currently used in sea ice VP models, hold~~(Ringeisen et al., 2019, 2021)~~? Second, does the observed IAD allows us to deduce the mechanical properties of sea ice and thereby constrain the shape of the yield curve or the plastic potential? To answer these questions, we see the need to revisit the IAD as it is presented in the literature. First, the angles reported in previous studies are given in the interval between 0 and 90°, leaving undefined if

80   these angles are acute (between 0 and 90°) or obtuse (90 to 180°) compared to the principal stress direction. Both cases need to be separated as they are linked to different slopes of the yield curve/plastic potential, hence to different shapes of the yield curve/plastic potential (Ringeisen et al., 2019). Second, ~~we need to filter~~ following the approach from Hutter et al. (2022b), we consider only conjugate pairs of LKFs, i.e., intersecting LKFs that formed simultaneously under compressive forcing~~, which is challenging given non-continuous coverage with satellite observations~~.

85   In this paper, we use satellite-derived sea-ice drift and deformation to address the gaps outlined above. Deformation concentrates along the LKFs, and vorticity identifies the LKFs formed under compressive force. Tracking of the LKFs allows for identifying those that formed simultaneously. Therefore, we can distinguish between conjugate and non-conjugate intersection angles and discriminate between conjugate obtuse and acute intersection angles. We apply this method to the RGPS dataset and new high-resolution deformation data surrounding the 2019/2020 ~~MOSAiC~~ Multidisciplinary drifting Observatory for the

90   Study of Arctic Climate (MOSAiC) expedition. Both datasets have different temporal and spatial coverage and resolution; thus, they indicate if intersection angles vary in the ice cover depending on the spatial scale and geographical location in the Arctic.

We aim to obtain an IAD as a reference for high-resolution sea ice models and to infer the mechanical properties of the sea ice cover, e.g., the yield condition and/or the plastic potential.

The remainder of this paper is structured as follows: Section 2 presents the different datasets used in this study (Section 2.1) and the algorithm for the measurements of the angles between 0 and 180° (Section 2.2). Section 3 presents the results of the intersection angles for the different datasets, the divergence along LKFs, seasonal variations, estimations of internal angles of friction, and an estimation of the shape of a yield curve for sea ice modelling. Discussion and Conclusions follow in Section 4 and 5.

2 Methods and data

2.1 Datasets

In this study, we will use two satellite-based sea-ice drift datasets from which sea-ice deformation is derived. Thanks to the synthetic aperture radar (SAR) data from which the drift is calculated, the datasets are available independent of weather conditions and during the polar night. The high spatial resolution (1.4 km ~~.~~ for MOSAiC and 12.5 km for RGPS) of the deformation datasets enables us to identify individual LKFs.

2.1.1 RADARSAT Geophysical Processor System

RGPS is a widely used drift and deformation dataset based on RADARSAT SAR images ~~(Kwok, 1998)~~(Kwok et al., 1998). The dataset covers the Amerasian Basin of the Arctic Ocean (Fig. 1) for twelve winters from 1996 to 2008. Sea ice drift is derived by tracking points that are spaced 10 km apart in SAR images. Deformation rates are computed from these Lagrangian drift paths and are interpolated to a regular 12.5 km grid. Hutter et al. (2019a) applied detection and tracking algorithms to the regular gridded data set and extracted deformation features, which are publicly available ~~(Hutter et al., 2019)~~ (Hutter et al., 2019b) and are closer analyzed in this study.

2.1.2 Sentinel (MOSAiC)

In addition, we compute ice drift and deformation based on Sentinel-1 SAR scenes (von Albedyll and Hutter, submitted). We base this dataset on HH-polarized scenes with a spatial resolution of 50 m. The scenes are located along the drift of the ~~Multidisciplinary drifting Observatory for the Study of Arctic Climate (MOSAiC) expedition (Nicolaus et al., 2022b)~~ MOSAiC expedition (Nicolaus et al., 2022a) from October 5, 2019, to July 14, 2020, except for the period between January 14 and March 15, when the ship was north of the satellite coverage (Figure 1). Typically, the time between two scenes was one day, with a few exceptions of 2-3 days, and the size of the scenes was on average 200×200 km. We compute ice drift fields based on a pattern-matching ice tracking algorithm introduced by Thomas et al. (2008, 2011) with substantial modifications by ~~Hollands and Dierking (2011a)~~Hollands and Dierking (2011b). We retrieve divergence, shear, total deformation, and vorticity
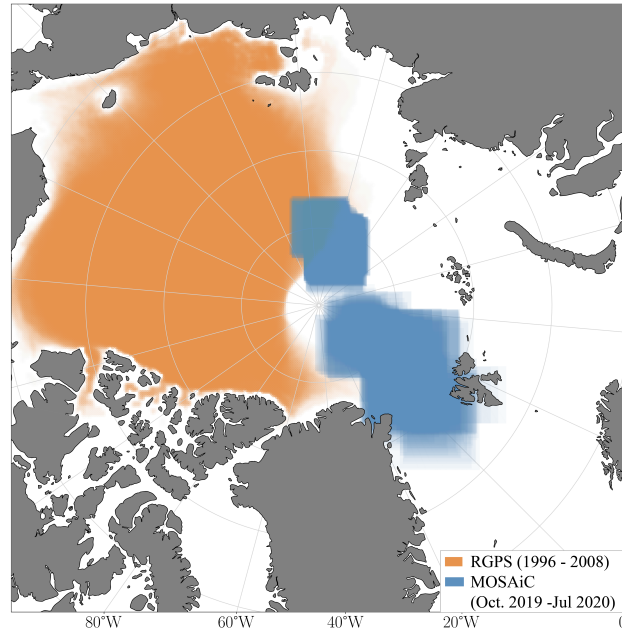
Figure 1. Coverage of the RGPS and MOSAiC LKF datasets. For the RGPS dataset, the transparency indicates the relative frequency of the coverage in the respective geographical regions.

from the regularly gridded sea-ice drift output at 1.4 km resolution following the approach described in von Albedyll et al. (2020) and Krumpen et al. (2021b).

2.2 LKF detection and Angles measurement

2.2.1 LKF detection

125 We use the algorithms presented in Hutter et al. (2019a) to detect and track LKFs in both deformation data sets. Here, we provide a short summary of the algorithms and direct the interested reader to the details in Hutter et al. (2019a). LKFs are detected in four steps: (1) pixels are marked as LKF if their deformation rates exceed the average deformation rate of the neighboring pixels, (2) all LKFs in the binary mask of LKF pixels are reduced to their skeleton using morphological thinning, (3) the binary map is divided into smallest possible LKF segments, and (4) segments are reconnected to one LKF based on

130 the probability of them belonging to the same LKF that is computed from their distance, orientation, and deformation rate magnitude differences. Next, the drift data is used to advect LKFs and track them over time. Note that to exclude a direct influence of the coast, those regions are excluded from the RGPS dataset, while the MOSAiC dataset only covers pack ice (see Fig. 1).

For RGPS, we use the publicly available ~~LKF data (Hutter et al., 2019)~~ deformation data (Hutter et al., 2019b) using the

135 original version of the code (Hutter, 2019). For the higher resolution MOSAiC ~~Sentinel~~ data, we add two modifications to the

original version of the detection code: (1) We apply a directional filter to the input deformation rates to reduce grid-scale noise. The directional filter is a 1-d kernel spanning 7 pixels that is ~~applied along~~ rotated at each pixel over all directions to compute the variability along different directions. We choose the direction of lowest variability ~~at each pixel to~~ to apply the 1-d filter and compute the filtered deformation rates. This allows us to reduce noise but still preserve the linear structure of LKFs in the deformation data. (2) The morphological thinning routine was modified to align the LKF skeletons in the binary maps to the position of the highest deformation rates across the LKF. The details of both modifications can be found in the routines in `dir_filter.py` in the newly released version of the code (Hutter, 2023)

2.2.2 Angles measurements

In both LKF datasets, pairs of LKF that intersect and are formed within the same time step are extracted, and the angle of intersection is measured following the approach of Hutter et al. (2019a) and ~~Hutter et al. (2022a).~~ Hutter et al. (2022b). The angles are measured from points ca. 10 points away (in both directions) from the intersection point, to avoid the effects of discrete orientations on a grid. In practice, because some LKFs are shorter, the number varies from 7 to 21 points. The number of 10 points was chosen to be a good compromise to get an accurate result and avoid discrete effects.

To differentiate between intersection ~~angle~~ angles that are acute ($< 90°$) or obtuse ($> 90°$), we use the vorticity $\left(\dot{\epsilon}_{\mathrm{vort}} = \frac{1}{2} \left(\frac{\partial u_1}{\partial x_2} - \frac{\partial u_2}{\partial x_1} \right) \right)$ along the LKFs as shown on Figure 2. From the vorticity information, we separate the data set into two categories: The conjugate angles (acute and obtuse together) and the non-conjugate angles. For conjugate angles, the ~~major~~ principal stress direction can be identified from the ~~ice motion indicated by the opposite sign~~ resulting ice motion. The ice flows from the most compressive to the least compressive principal stress. Note, by convention, as compression is negative, the first principal stress direction is the direction with the lower compressive stress, while the second is the higher compressive stress. We do not consider the exact stresses here but only the principal stresses and their direction, therefore it includes also bidirectional compression situations. The motion becomes obvious from the opposite sign of the vorticity along the intersecting LKFs (Fig. 2). In other words, for a conjugate pair of LKFs, the vorticity alternates between positive and negative along the segments of the two intersecting LKFs. For equal sign vorticity along both LKFs, the ice motion field does not allow identifying the main stress direction, and we classify the intersecting pair as non-conjugate.

While the generation of conjugate faults is explained by the failure of ice under compressive loading, the reasons for the existence of non-conjugate failure are less obvious. We show the distribution of the non-conjugate angles and explore reasons for these non-conjugate faults in Appendix A.

3 Results

In the following sections, we present the results of our investigation of intersection angles in both MOSAiC and RGPS data sets. We compare the intersection angles distribution (IAD), the relationship between angles and dilatancy, and how these distributions inform us about sea ice dynamics, especially the internal angle of friction, and the possible shape of the yield curve or the plastic potential for sea ice VP models.
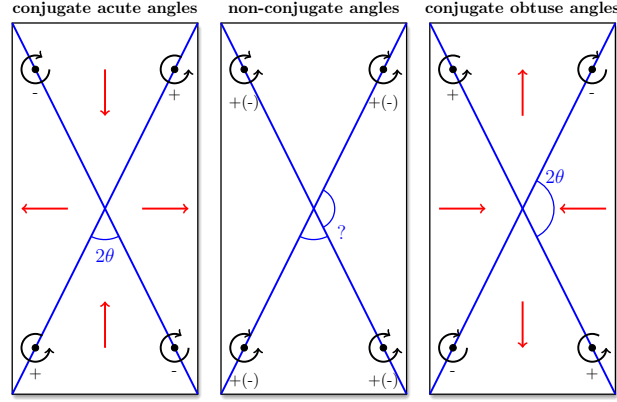
Figure 2. Schematics showing the difference between conjugate failure lines with acute and obtuse angles, and with non-conjugate failure lines. The vorticity of the ~~drift allows~~ ice motion (black circles with $+/-$ signs) indicates the direction of the principal stresses (red arrows), hence making the difference between conjugate (left and right panels) and non-conjugate (middle panel) failure lines.

3.1 Example of LKFs intersection

Figure 3 presents three examples of LKFs intersections from the MOSAiC data set, one conjugate acute angle (Fig. 3a), one conjugate obtuse angle (Fig. 3c), and one non-conjugate angle (Fig. 3b). Especially for conjugate acute angles, we observe that LKFs with the same orientation have vorticities of the same sign ~~.~~ (Fig. 3a). These patterns agree with the concept of fracture in diamond shapes as shown in DEM simulation ~~(Wilchinsky et al., 2010) or~~ (Wilchinsky et al., 2010; Heorton et al., 2018) and in theoretical works (Pritchard, 1988). For the non-conjugate and the obtuse angles, the fracturing pattern is more chaotic, a possible effect of heterogeneities in the ice strength, e.g., in the ice thickness field or rapidly changing forcing fields.

In the following, we focus on intersection angles between conjugate LKFs, which we can classify as acute or obtuse. We include only LKFs that formed during the same time step of observation.

3.2 Intersection angles

Figure 4 shows the probability density function (PDF) of the intersection angle of conjugate LKFs for the MOSAiC and RGPS datasets. The PDF of both datasets agrees remarkably well. Both IAD peak at acute angles, with a modal value in the range between 40° and 50°. Also, we find only a few large angles. For both datasets, around 80% of the conjugate angles are acute with around 25% of the conjugate angles ranging between 30° and 60°.

~~We fit both IAD~~ To characterize the PDF, we fit both PDFs to an exponentially modified Gaussian (exGaussian) distribution with a Maximum Likelihood Estimator (MLE). The parameters of the fit are given in the caption of Fig. 4. The formula of the exGaussian distribution is,

$$f(x; \mu, \sigma, \tau) = \frac{1}{2\tau} e^{\frac{1}{2\tau}\left(2\mu + \frac{\sigma^2}{\tau} - 2x\right)} \operatorname{erfc}\left(\frac{\mu + \frac{\sigma^2}{\tau} - x}{\sqrt{2}\sigma}\right), \tag{1}$$
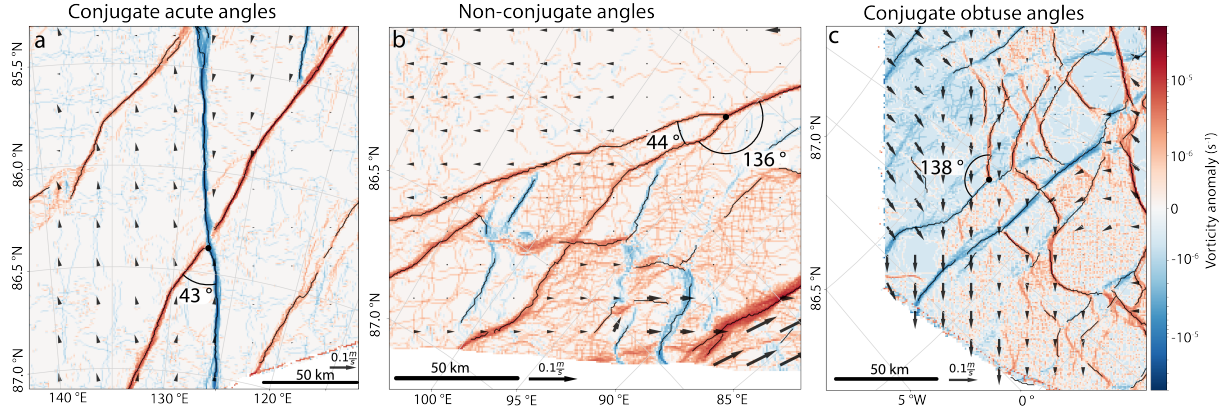
Figure 3. Example of LKFs intersections with the vorticity anomaly and sea ice drift within the MOSAiC dataset. Panel **(a)** shows an intersection with an acute angle (Jan 1-2, 2020), panel **(b)** shows an intersection with a non-conjugate angle (Nov 11-12, 2019), and panel **(c)** shows an intersection with an obtuse angle (Mar 15-16, 2020). The arrows indicate the velocity anomaly of the sea ice drift calculated for the displayed data. Detected LKFs are plotted as thin black lines. The colorbar of the vorticity anomaly is the same for all panels.

with

$$\text{erfc}(x) = \frac{2}{\sqrt{\pi}} \int\limits_{x}^{\infty} e^{-t^2} \, dt. \tag{2}$$

The goodness of the fit is tested with a Monte-Carlo test with 10 000 ~~iterations~~ different random sub-samples, taking into account the discrete nature of intersection angles between LKFs that are defined on a regular grid ~~(Clauset et al., 2009; Hutter et al., 2019a)~~
190 (Hutter et al., 2019a), and using a Kolmogorov–Smirnov (KS) statistic (see details in Clauset et al., 2009; Hutter et al., 2019a)
. We also tested the Logarithmic Normal Distribution and the Skew Normal Distribution, but these fits failed the Monte-Carlo test. The fitted exGaussian distributions show a modal peak at $49° \pm 1°$ for the RGPS dataset and $42° \pm 4°$ for the MOSAiC dataset (Figure 4). Considering the different spatial and temporal resolutions as well as the different ice regimes sampled, this agreement is remarkable and allows us to generalize conclusions on sea ice properties.

195 The PDF of intersection angles does not vary seasonally for the RGPS dataset. For the MOSAiC dataset, there are too few intersection angles to study seasonal variations (not shown). Appendix A presents and discusses the PDF of non-conjugate intersection angles.

3.3 Divergence and convergence along leads

~~Besides the~~ We extract the deformation rates from all pixels defined as part of a LKF to compare the characteristics of the
200 deformation in the MOSAiC and RGPS dataset. Like for the IAD, both the MOSAiC and the RPGS dataset agree in the shape of the distribution of the divergence, shear, and total deformation rates along LKFs (Fig. 5a, b, and c, respectively). Since RGPS and MOSAiC differ in spatial resolution by one order of magnitude and deformation rates are known to be scale-dependent, we normalize the divergence and shear to compare the relative frequencies. On average, we find more divergent ice motion along
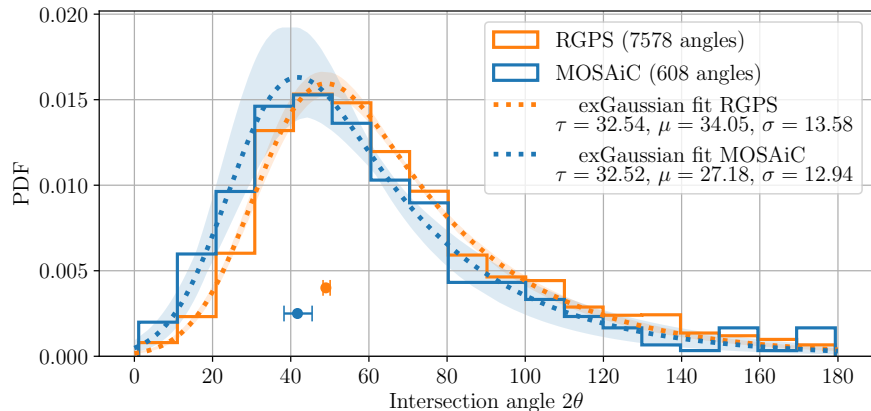
Figure 4. Probability density function of the conjugate intersection angles for the MOSAiC (blue) and RGPS (orange) datasets. The dashed lines show the MLE fit to an exponentially modified Gaussian (exGaussian) distribution (Eq. 1), where the fitted distribution parameters are shown in the legend. The shading shows the 1-σ error of the distribution fits. We show the position of the distribution's peak with its 1-σ error: $49° \pm 1°$ for the RGPS dataset and $42° \pm 4°$ for the MOSAiC dataset.

LKFs in the MOSAiC data set compared to the RGPS data set (Fig. 5~~b), which can be explained by the~~ a). We speculate that this reflects a generally more divergent regime in the Transpolar drift compared to the Beaufort Gyre ~~that~~ which features more compressive settings~~(Fig. 1).~~. The RGPS data set shows higher shear deformation that ~~originates~~ could potentially originate from the circular motion of the Beaufort Gyre. The higher shear rates also result in higher total deformation rates in the RGPS data set. We can calculate the dilatancy angle along the LKF, δ, i.e., the angle of deformation defined by the ratio of shear and divergence $\tan(\delta) = \frac{\dot{\epsilon}_\mathrm{div}}{\dot{\epsilon}_\mathrm{shear}}$ (Tremblay and Mysak, 1997). Here, the divergence and shear are used before normalization. The presence of smaller dilatancy angles in the distribution (Fig. 5d) shows well that divergence is more frequently occurring in the MOSAiC dataset (Fig. 5d).

Further, we analyze the relationship between intersection angles and dilatancy angles (Figure 6). We find a weak correlation between the intersection angle and the dilatancy angle, with a correlation coefficient $\rho = -0.5$ for MOSAiC, and a very weak correlation $\rho = -0.2$ for RGPS. The theory of Roscoe angles θ_R (Roscoe, 1970) states that the dilatancy (~~that is~~i.e., the orientation of the flow rule) controls the orientation of the LKFs. In doing so, intersection angles 2θ can be described as a function of the dilatancy angle δ and vice versa by

$$2\theta = \arccos(\tan(\delta)) \tag{3}$$

shown as a red dashed line in Figure 6. In contrast to theory, we find that both PDFs are not linked following this functional form (Figure 6), showing only weak correlations ($\rho_R = 0.46$ for MOSAiC and $\rho_R = 0.20$ for RGPS) and even negative determination coefficients R^2, meaning that a constant line would be a better fit than Eq. (3).
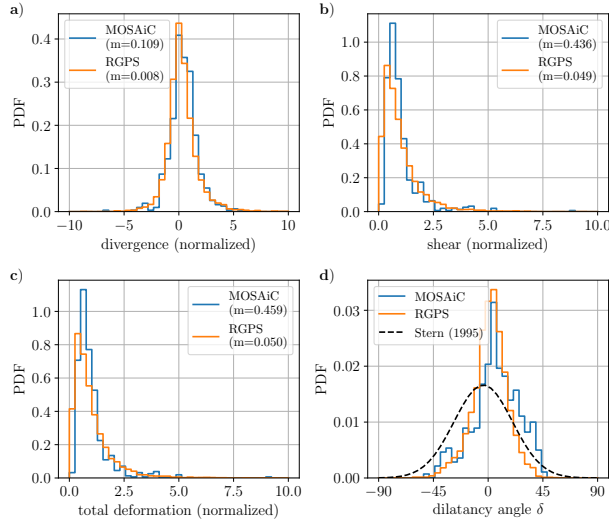
Figure 5. Probability distribution function of normalized convergence **(a)**, normalized divergence **(b)**, and normalized total deformation **(c)** along failure lines, as well as the dilatancy angle $\delta = \tan^{-1}\left(\frac{\dot{\epsilon}_{\mathrm{div}}}{\dot{\epsilon}_{\mathrm{shear}}}\right)$ **(d)**. The means used for the normalization are given in parentheses in the legend. The black curve on panel **(d)** shows the Gaussian curve with the parameters presented in Stern et al. (1995, their Fig. 4) for comparison.
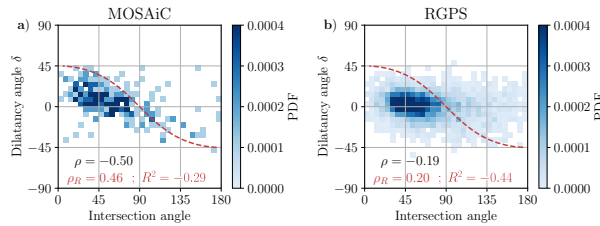
Figure 6. Scatter plot of the dilatancy angles δ versus the intersection angles between LKFs. The correlation between the intersection angle and the dilatancy angle is $\rho = -0.5$ for MOSAiC and $\rho = -0.19$ for RGPS. The red dashed line shows the relationship between dilatancy and angles expected following a normal flow rule or the Roscoe angle theory. The correlation between this prediction and the observed dilatancy angles are $\rho_R = 0.46$ for MOSAiC and $\rho_R = 0.20$ for RGPS. All correlations are significant.

These findings contradict the concept of the Roscoe Angle θ_R and the idea of a normal flow rule, as we observe only weak correlations between intersection angles and dilatancy angles. We, however, note that the MOSAiC dataset holds a higher correlation than the RGPS dataset. The non-correlations could arise from an observational bias due to the low temporal resolution. Increasing the temporal resolution might show a correlation as it would resolve the deformation just after failure.

225 Finally, we note that our observations confirm the theoretically expected range of the dilatancy angle: As expected from Roscoe's theory and the normal flow rule condition, dilatancy angles lower than $45°$ and above $135°$ are very rare in our observations (Fig. 6 and Fig. 5d).

3.4 Mechanical properties of sea ice

3.4.1 Estimation of the internal angle of friction

230 The peak of the IAD shows a preferred angle of failure of sea ice that can be used to estimate the internal angle of friction of sea ice within the framework of the Mohr–Coulomb failure criterion (Coulomb, 1776). The internal angle of friction is the ratio of shear stress τ and normal stress σ at which the material yields.

The internal angle of friction is given by $\phi = \frac{\pi}{2} - 2\theta$, where 2θ is the peak of the IAD. Within the Coulombic framework, the internal angle of friction is linked to a Coulombic shear criterion, such as

235
$$\tau = \mu\sigma + \tau_0 \tag{4}$$

with $\mu = \tan(\phi)$ .and where τ_0 is the cohesion, i.e., the shear strength . Similarly, the criterion can be translated in invariant stress space (σ_I, σ_{II}) for the construction of a yield curve (Ringeisen et al., 2019) and is given by

$$\sigma_{II} = \mu_I\sigma_I + c_I. \tag{5}$$

with $\mu_I = \sin(\phi)$.

240 Using these formulas with the observed IAD from our study, we find:

- The peak intersection angles for the RGPS dataset of $2\theta = 49° \pm 1°$ implies an internal angle of friction of $\phi = 41° \pm 1°$, $\mu = 0.87 \pm 0.03$, and $\mu_I = 0.66 \pm 0.02$.

- For the MOSAiC dataset, the intersecting angle of $2\theta = 42° \pm 4°$, we get $\phi = 48° \pm 4°$, $\mu = 1.12 \pm 0.15$, and $\mu_I = 0.75 \pm 0.05$.

245 (By following the framework of Erlingsson (1988, 1991), a breaking index of $i = 2$ gives internal angles of friction of $\phi \simeq 25°$ and $\phi \simeq 65°$.)

Note that for this calculation, we only take the peak of the IAD into account, neglecting the presence of other intersection angles in the PDF.

3.4.2 Estimation of the shape of a yield curve or a plastic potential

Instead of using only a single angle to derive the mechanical properties of sea ice, we can also use the complete PDF of the intersection angles (Figure 4) to create an approximation of the shape of the yield curve or plastic potential within the viscous-plastic framework. Below, we consider that the curve that we derive can be a yield curve or a plastic potential because it is still an open question of which of these mechanical properties set the intersection angles of LKFs in sea ice plastic models. There are indications that the plastic potential could be responsible (Ringeisen et al., 2021). To reconstruct these curves from the IAD, we follow the results of (Wang, 2007), Ringeisen et al. (2019), or Ringeisen et al. (2021). The slope of different parts of the yield curve (Coulomb angle) or plastic potential (Roscoe angle) are linked to different intersection angles:

$$
2\theta = \arccos\left(-\frac{\partial F_{\mathrm{I}}}{\partial \sigma_{\mathrm{I}}} \frac{\partial \sigma_{\mathrm{II}}}{\partial \sigma_{\mathrm{I}}} \right) \tag{6}
$$

where the function $F_{\mathrm{I}} = \sigma_{\mathrm{II}}(\sigma_{\mathrm{I}})$ defines the yield curve or the plastic potential in the invariant stress space ($\sigma_{\mathrm{I}},\sigma_{\mathrm{II}}$). In the following, we make the hypothesis that the number of intersecting LKFs within a bin of angles is proportional to the length of the yield curve/plastic potential curve that creates this angle. Here, our underlying hypothesis is that all the points on the yield curve/plastic potential are equally likely. An additional constraint is that the curve is required to be convex to agree with the convexity condition of Drucker's postulate of stability (Drucker, 1959).

For each bin of angles in the PDF of the intersection angles (Figure 4), we compute a segment of the yield curve (or plastic potential) that has the length of the PDF value and the slope given by the angle in the center of this bin θ_m, given by

$$
\frac{\partial \sigma_{\mathrm{II}}}{\partial \sigma_{\mathrm{I}}} = -\cos(2\theta) \tag{7}
$$

from inverting Eq. (6). This process is illustrated on Fig. 7. We start the construction of the curve at the origin of the invariant stress $(\sigma_{\mathrm{I}}, \sigma_{\mathrm{II}}) = (0,0)$. We start from the smallest intersection angles of the distribution, as they are linked to the steepest curve slopes from Eq. 7, and iterate through the PDF, with the start point of each segment being the tip of the previous segment. Note that as long as the intersection angles are either monotonically increasing or decreasing, our method necessarily leads to a convex yield curve. Finally, the curve values are normalized to have the tip at $\sigma_{\mathrm{I}} = -1$. Figure 8 shows the resulting shape.

The estimation of the obtained curves for the RGPS and MOSAiC dataset resemble a teardrop yield curve (Zhang and Rothrock, 2005; Rothrock, 1975; Ringeisen et al., 2022), a Mohr–Coulomb yield curve (Ip et al., 1991), or (to a lesser extent) the curved diamond yield curve (Wang, 2007), but clearly deviate from the elliptical yield curve (see Appendix B). For comparison, we added a teardrop, a Mohr–Coulomb, and a curved diamond yield curve in Fig. 8.

Note that the starting point of our curve is arbitrarily placed at the origin, as we did not consider tensile strength. However, adding tensile strength would not change the shape of the curve, which is central, but only the actual values of σ_{I}, σ_{II}. In other words, the shape of the curve is important, and not its position in the (σ_{I}, σ_{II}) space.
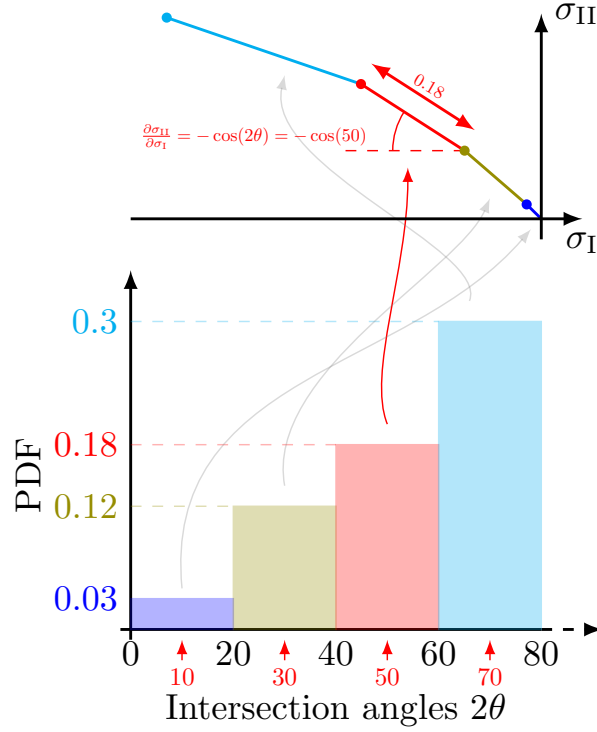
Figure 7. Example of the approximation method for the yield curve or plastic potential from the intersection angles distribution (IAD). Each bin of the distribution is used to create a segment of the curve with the length of the PDF value and the angle corresponding to the center of the bin, starting from the smaller bin.

In Appendix B, we present a proof-of-concept of this method. Using the IAD measured in three 2 km simulations with the Massachusetts Institute of Technology general circulation model ~~(MITgcm, Hutter et al., 2022a)~~ (MITgcm, Hutter et al., 2022b) we show that the yield curves reconstructed with the presented method agree well with the elliptical yield curves used in the simulations.

4 Discussion

We show the intersection angle distribution (IAD) of conjugate faults in the Arctic sea ice during faulting events. The IAD shows the predominance of small intersection angles of $30°$ to $60°$. The predominance of small angles agrees with the previous observations of intersection angles, which report angles between $28°$ and $36°$ (Erlingsson, 1988; Marko and Thomson, 1977; Walter and Overland, 1993; Cunningham et al., 1994). However, our observations show that also wider angles, and even obtuse angles, are present in sea ice, although less frequently. The spread and shape of the IAD can be explained by the presence of heterogeneities in the ice (open or refrozen leads, ridges, polynyas) that influence the orientation of
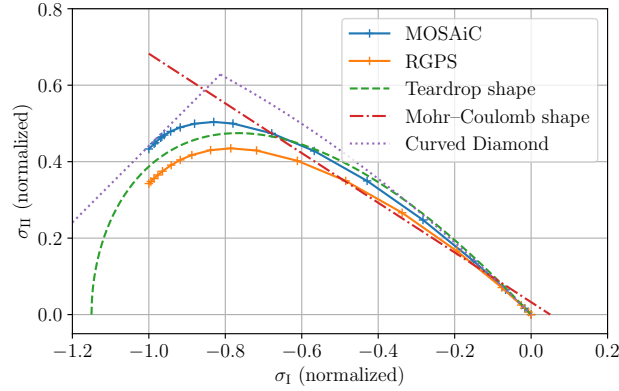
Figure 8. Yield curve/Plastic potential constructed from the PDF of the intersection angles. The red dash-dotted line, the green dashed line, and the dotted violet line ~~show~~ shows a Mohr–Coulomb yield curve (Tremblay and Mysak, 1997), a teardrop shape (Zhang and Rothrock, 2005; Ringeisen et al., 2022), and a curved diamond (Wang, 2007), respectively, for comparison. For the Mohr–Coulomb yield curve, the slope is $\mu = 0.75$, as derived in Sec. 3.4.1

LKFs~~Wilchinsky and Feltham (2011)~~(Wilchinsky and Feltham, 2011), or by variations of internal confining pressure (Golding et al., 2010; Schulson et al., 2006). The heterogeneities serve as the preferred direction of ice failure and, therefore, can alter the intersection angle from the single angles of Mohr–Coulomb theory. We note that the IADs of the RGPS and MOSAiC datasets look very similar in shape. Given the different scales, times, and regions of the datasets, we conclude that the shape of the IAD seems to be a characteristic of sea ice. ~~We wonder~~ Future work should investigate how the shape of the IAD is linked to other typical characteristics of sea ice, like the shape of the floe size distribution (Rothrock and Thorndike, 1984; Stern et al., 2018) and the shape of the ice thickness distribution (von Albedyll et al., 2022; Thorndike et al., 1975).

Using the peak of the IAD, we made an estimation of the internal angle of friction from the Mohr–Coulomb's framework. Our estimates of $\mu_I = 0.66$ and $\mu = 0.75$ agree well with previous estimates of the internal angle of friction $\mu \in [0.6, 0.8]$ ~~(Schulson et al., 2006).~~ by (Schulson et al., 2006). In contrast, our estimates disagree with the findings of Erlingsson (1988, 1991). Applying a breaking index of $i = 2$ defined by his methodological framework, the estimated internal angles of friction are $\phi \simeq 25°$ or $\mu \simeq 0.13$ and $\phi \simeq 65°$ or $\mu \simeq 0.82$. However, since we find that this framework does not agree with the creation of LKFs in sea ice models, we rather focus on the Mohr–Coulomb's framework. More importantly, we used the IAD to derive an approximation of a yield curve/plastic potential for sea ice VP models. Wang (2007) used a similar method to create the Curved Diamond yield curve, but with fewer angle observations and the strong assumption about inferring the unknown stress direction from coastal geometry. Using the along-lead vorticity, we ~~do not need to make this assumption~~know the main stress direction and can do without such assumptions. The shape resulting from our analysis is similar to a teardrop shape (Rothrock, 1975; Zhang and Rothrock, 2005; Ringeisen et al., 2022), a Mohr–Coulomb shape (Ip et al., 1991), or to a lesser extent, a Curved Diamond (Wang, 2007). In contrast, the shape we obtain does not fit the elliptical shape (Hibler, 1979) or the Parabolic

310   Lens shape (Zhang and Rothrock, 2005). These findings are of great relevance for designing new rheologies for sea ice models~~, and~~. In this context, the observed IAD can be also used as a metric to assess the models' capability to represent LKFs.

    In VP models, the orientation of the LKFs is tightly linked to the flow rule, i.e., the dilatancy or post-failure deformation, at least for the elliptical yield curve and plastic potentials Ringeisen et al. (2021). The observations presented here show no strong relationship between the observed dilatancy angle and the observed intersection angle, nor between the dilatancy angles

315 and the expected angles from Roscoe theory (Roscoe, 1970) or the normal flow rule. We consider insufficient observations or a general flaw in the VP rheological framework as potential reasons for this misfit between theory and observations. First, the temporal resolution of our observations might be insufficient to resolve double sliding cycles with positive and negative dilatancy (Balendran and Nemat-Nasser, 1993). In that case, we would not see the immediate post-fracture deformation, but the sliding of ice packs that alternate between dilatation and compression. This would lead to a random distribution of dila-

320 tancy angles and, thus, a de-correlation. We suggest further observational studies with a higher temporal resolution to confirm the de-correlation. Second, if confirmed by observations at higher temporal resolution, uncoupling between dilatancy and intersection angles would mean that the intersection angle is not influenced by the velocity characteristics of the medium. A confirmed uncoupling would question the capacity of the VP rheological framework to reproduce both the dilatancy and the LKFs intersection angles simultaneously.

325   The presented results of the IAD are robust in scale, resolution, and geographic area. The RGPS dataset has low spatial and temporal resolution but a large spatial and time coverage, whereas the MOSAiC dataset has higher resolution, but only covers the track of the MOSAiC drift experiment. The scale independence of the intersection angles agrees with the self-similarity and scaling properties of sea ice deformation ~~(Marsan et al., 2004a; Rampal et al., 2008; Hutchings et al., 2011a; Weiss, 2013; Bouchat and Tre~~ (Rampal et al., 2008; Weiss, 2013; Marsan et al., 2004b; Bouchat and Tremblay, 2020b; Hutchings et al., 2011b). While the LKFs

330 at the kilometer scale resolution that we analyzed in this study are mostly systems of smaller-scale leads, the question remains if the observed deformation characteristics and IAD are still present at the floe scale ($< 100\,m$). Observational scaling studies analyzing sea ice deformation derived from ship-radar have shown that sea ice deformation follows the same scaling behavior down to scales of $50\,m$ ~~(Oikkonen et al., 2017a)~~(Oikkonen et al., 2017b). This and laboratory experiments at sub-meter scale (Schulson et al., 2006; Weiss and Dansereau, 2017) indicate similar failure behavior across scales and, therefore, no scale-

335 break. However, scaling characteristics are known to be only weakly linked to the representation of LKF intersection angles ~~(Hutter et al., 2022a)~~ (Hutter et al., 2022b) and therefore are potentially a poor proxy for the floe-scale IAD. Deformation derived from the shipborne ice radar from the MOSAiC drift experiment could bridge the gap in the scale analysis of the LKFs intersection angle and give insight into small-scale processes involved (rotation, reopening of leads) thanks to its high-temporal ($2\,sec$ - $10\,min$) and spatial ($10\,m$) resolution in the proximity (approx. $9\,km$) of the ship (Krumpen et al., 2021a).

340 ## 5 Conclusions

Using the vorticity in sea ice deformation, we show that we can separate obtuse and acute intersection angles between sea ice Linear Kinematic Features (LKFs). Using this technique, we can now extract the Probability Density Function (PDF) of the

intersection angles between 0 and 180°, instead of being limited to the range between 0 and 90°. We investigate intersection angles within two different deformation datasets: the RADARSAT RGPS product ~~(Hutter et al., 2019)~~(Hutter et al., 2019b),

345 and the MOSAiC dataset from Sentinel-1 A/B (von Albedyll and Hutter, submitted).

The PDFs of intersection angles show that acute angles dominate in both datasets, with PDFs peaking at 48°(RGPS) and 45°(MOSAiC). Both PDFs are described by an exponentially modified Gaussian that agrees remarkably in shape~~, i. e.,~~. We therefore conclude that the Intersection Angle Distribution (IAD) is scale invariant. The distributions of divergence and shear rates along the LKFs also agree when taking the scaling of deformation rates into account. Both indicate scale-invariant

350 behavior of fracture mechanics and intersection angles that remain to be tested at the floe scale. We do not find a relationship between the dilatancy angles along the leads and their corresponding intersection angles, which could be an artifact of the temporal resolution of a minimum of one day that might "smear" the deformation during instantaneous failure with post-fracture sliding. If not falsified with deformation data at very high temporal resolution, e.g., ship radar, the de-correlation of dilatancy and intersection angles contradicts the normal flow rule assumption used within the VP framework.

355 We infer the mechanical properties of sea ice from the observed IAD. Following methods from previous papers, we estimate the internal angle of friction at ~~$\mu_I = 0.66 \pm 2$~~$\mu_I = 0.66 \pm 0.02$ and $\mu_I = 0.75 \pm 0.05$ from the PDF peak for the MOSAiC and the RGPS datasets, respectively. We outline a new method to derive the shape of the yield curve/plastic potential from the shape of the intersection angles PDF. The resulting shape agrees well with the shape of the teardrop yield curve (Zhang and Rothrock, 2005; Ringeisen et al., 2022), the Mohr–Coulomb curve (Ip et al., 1991), and to a lesser extent, the Curved Diamond

360 (Wang, 2007). We conclude that the popularly used elliptical yield (Hibler, 1979) is not backed by our observations.

Reproducing the observed patterns of LKFs in the Arctic sea ice is one of the remaining challenges of the sea ice modeling community ~~(Hutter et al., 2022a)~~(Hutter et al., 2022b). We provide here an observed IAD that can be used as a metric for the evaluation of models, and we suggest replacing the elliptical yield curve in VP models with a teardrop yield curve for a better representation of simulated LKFs. Such a new setup will need to be tested in high-resolution Arctic simulations to determine

365 if it represents the IAD observed in this study accurately.

Code and data availability. The deformation data based on Sentinel-1 SAR imagery is made available on PANGAEA under the identifier: PDI-33705 (von Albedyll and Hutter, submitted). The RGPS LKF data is available available on PANGAEA (Hutter et al., 2019b). The LKFs extraction code is available on Zenodo (Hutter, 2019) and we will be updated after the review process (Hutter, 2023)

370 The python code to create possible yield curves from intersection angles PDF (and inversely) is available on request and will be made available publicly after the review process.

Appendix A: Non-conjugate angles

In Sect. 3.4.1, we show that for 37% of the intersection angles (28% for MOSAiC and 38% for RGPS), it is possible to separate the acute and the obtuse angles. However, for many intersecting LKFs, the LKFs' vorticities are the same and it is not possible to separate between obtuse and acute angles (see Figure 2b). Figure A1 shows the IAD for all angles, conjugate angles, and
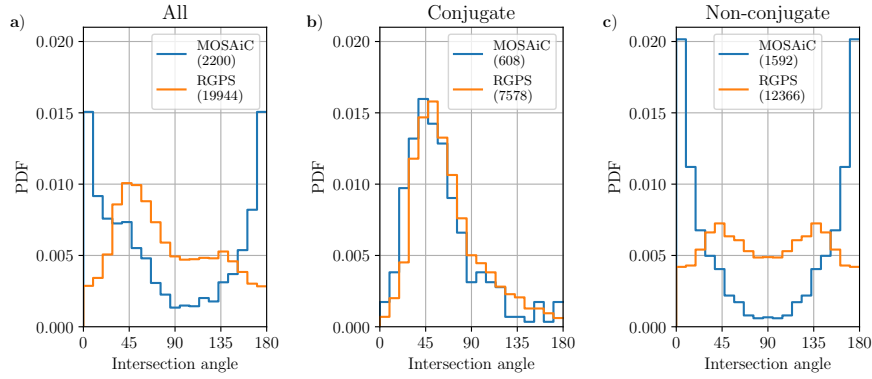
Figure A1. Probability Density Function (PDF) of the intersection angles in the Arctic sea ice. The panels show the conjugate and non-conjugate angles for all (left), Conjugate (middle), and non-conjugate (right) angles, as defined on Fig. 2. The numbers in parenthesis show the numbers of intersection angles shown in the PDF.

non-conjugate angles. Note that these PDFs are mirrored relative to 90°, as we cannot differentiate between obtuse and acute angles. For the RGPS dataset, extracting the non-conjugate angles leads to a very uniform IAD: there is still a peak in the IAD, but it is much less dominant. For the MOSAiC dataset, the non-conjugate angles feature many small angles, with peaks around 0°and 180°.

The intersecting LKFs with the same vorticity can have several origins:

1. The time step of the observations is too large to resolve the actual vorticity during the deformation. The vorticity recorded over a (multi-)day period is not necessarily representative of the deformation rates during the formation. Even if two intersection LKFs are formed under compressive forcing, rapidly changing winds can induce a different ice motion. In this case, the initial failure allows the more mobile ice to deform in shear motion, which leads to the same vorticity sign. This behavior may be especially present for deformation data with a low temporal resolution, e.g., the RGPS dataset.

2. The presence of the same vorticity sign on both intersecting LKFs could emerge from rotation. LKFs dynamics can involve rotation under shear (Wilchinsky and Feltham, 2004), a process also observed in granular materials (e.g., Oda and Kazama, 1998). This process seems more likely for small-scale observations, e.g., from the ~~MOSAIC Sentinel~~ MOSAiC dataset with a spatial resolution of 1.4 km.

3. If an LKF is not detected properly and cut into two parts, both parts will have the same sign vorticity, and due to their proximity, will be identified as intersecting LFKs in our analysis. We tuned the parameters of the detection algorithms to minimize this effect, but especially for the MOSAiC data, we find instances of this effect.

Appendix B: Fracture angles from the elliptical yield curve

~~We inverse the process of Sect. 3.4.2 to extrapolate the intersection angles that would be given by the elliptical curve (yield curve or plastic potential) in the VP sea ice model. This way, we can~~ In this appendix, we show, as a proof of concept, that the method used in Section 3.4.2 allows to reconstruct the shape of the elliptical yield curve from the model deformation output. First, we compute the theoretical intersection angles distribution from the yield curve shape. Then, we extract the intersection angles distribution from 2km resolution pan-arctic simulations. Finally, we reconstruct the yield curve shape from the modeled intersection angles distribution and show that it gives a shape very similar to the yield curve of the first step.

First, we compute the expected PDF of the intersection angles in a high-resolution sea ice viscous-plastic model that uses an elliptical yield curve ~~.~~ (Fig. B1a). For thousands of points on the yield curve, we compute the theoretical fracture angles, we then use these points to create a theoretical intersection angle distribution. Figure B1c shows the results of this process for three different aspect ratios e. The PDF of the intersection angles for $e = 2$ peaks strongly at $90°$. Using a smaller aspect ratio, such as $e = 0.7$ (Bouchat and Tremblay, 2017) flattens the PDF. These PDFs are symmetrical relative to $90°$ while the observations presented in this paper (Figure 4) are strongly skewed towards small angles. Note that this process to estimate the IAD still uses the assumption that all parts of the yield curve are equally probable to be the subject of plastic deformation. An analysis of high-resolution sea ice models would be necessary to see if this hypothesis is valid.

The histogram lines on Fig. B1c show the PDF of conjugate intersecting angles in a 2 km MITgcm simulation ~~(?)~~ (Hutter et al., 2022b) using the same method as described in Sect. 2.2. The histograms of simulated intersection angles show the same evolution of the PDF as expected from theory, with a higher peak around $90°$ for $e = 2$, and a flatter PDF for $e = 1.0$ and $e = 0.7$. Also, the PDFs of the models are close to being symmetrical with respect to $90°$, despite using the algorithm to separate obtuse and acute angles.

On Fig. B1d, we use the IAD from the simulations (Fig. B1c) to reconstruct the yield curve for all three values of e, as done in Sect. 3.4.2. The resulting yield curve fits well with the elliptical yield curve prescribed in the associated simulations. There is a larger difference for $e = 2$ case, intersection angles around $90°$ are less present than we would expect from the model. Globally, we see that all three PDF of the modeled intersection angles are missing angles around $90°$. This could be the results of a small departure from the hypothesis that all parts of the yield curve are equally probable. Note that LKFs intersection angles can only be created when the slope of the yield curve is within the range $[-1, 1]$. A slope of -1 corresponds to an intersection angle of $0°$, a slope of $+1$ corresponds to an intersection angle of $180°$. To take this into account, we start reconstructing the yield curve at the point $[\sigma_I, \sigma_{II}]$ where $\frac{\partial \sigma_{II}}{\partial \sigma_{II}} = -1$ $\frac{\partial \sigma_{II}}{\partial \sigma_I} = -1$, and scale the rest of the yield curve to have the endpoint at σ_I where the slope is $\frac{\partial \sigma_{II}}{\partial \sigma_{II}} = 1$ $\frac{\partial \sigma_{II}}{\partial \sigma_I} = 1$.

Author contributions. DR coordinated this study, derived the sea ice properties (internal angle of friction and curve shape), made figures, and wrote sections. NH performed the LKFs extraction, the intersection angles measurement and classifications for both data sets, made figures, and wrote sections. LvA provided the MOSAiC deformation dataset, made figures, and wrote sections. All authors edited the manuscript.
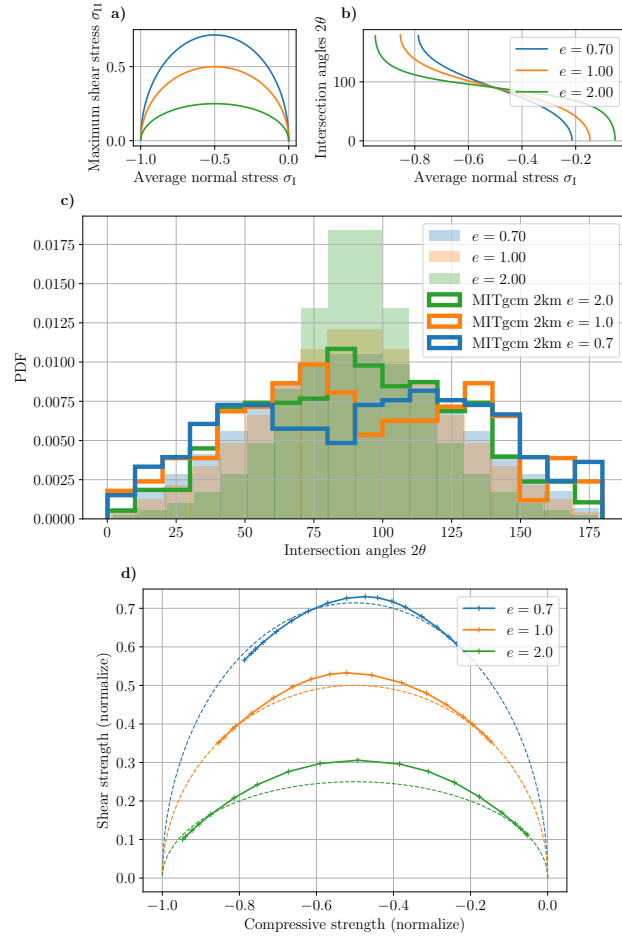
Figure B1. Elliptic yield curves in invariant space **(a)**, their theoretical fracture angle as a function of the first invariant σ_I **(b)**, the PDF of the theoretical fracture angles, with the PDF of conjugate intersection angles from MITgcm 2 km resolution runs for the same ellipse ratios **(c)**, and the reconstructed yield curve from the modeled IAD **(d)**.

Competing interests. The authors declare that they have no conflict of interest

425 *Acknowledgements.* The authors would like to thank Jennifer Hutchings, Daniel Watkins, and Bruno Tremblay for their comments on an earlier version of this work. This project has been supported by the Deutsche Forschungsgemeinschaft (DFG) through the International Research Training Group "Processes and impacts of climate change in the North Atlantic Ocean and the Canadian Arctic" (grant no. IRTG 1904 ArcTrain).

References

430 Balendran, B. and Nemat-Nasser, S.: Double sliding model for cyclic deformation of granular materials, including dilatancy effects, Journal of the Mechanics and Physics of Solids, 41, 573–612, https://doi.org/10.1016/0022-5096(93)90049-L, 1993.

Bouchat, A. and Tremblay, B.: Using sea-ice deformation fields to constrain the mechanical strength parameters of geophysical sea ice, Journal of Geophysical Research: Oceans, pp. n/a–n/a, https://doi.org/10.1002/2017JC013020, 2017.

Bouchat, A. and Tremblay, B.: Reassessing the Quality of Sea-Ice Deformation Estimates Derived From the RADARSAT Geophys-
435 ical Processor System and Its Impact on the Spatiotemporal Scaling Statistics, Journal of Geophysical Research: Oceans, 125, https://doi.org/10.1029/2019jc015944, 2020a.

Bouchat, A. and Tremblay, B.: Reassessing the Quality of Sea-Ice Deformation Estimates Derived From the RADARSAT Geophysical Pro-
cessor System and Its Impact on the Spatiotemporal Scaling Statistics, Journal of Geophysical Research: Oceans, 125, e2019JC015 944, https://doi.org/https://doi.org/10.1029/2019JC015944, _eprint: https://agupubs.onlinelibrary.wiley.com/doi/pdf/10.1029/2019JC015944,
440 2020b.

Bouchat, A., Hutter, N., Chanut, J., Dupont, F., Dukhovskoy, D., Garric, G., Lee, Y. J., Lemieux, J., Lique, C., Losch, M., Maslowski, W., Myers, P. G., Ólason, E., Rampal, P., Rasmussen, T., Talandier, C., Tremblay, B., and Wang, Q.: Sea Ice Rheology Experi-
ment (SIREx): 1. Scaling and Statistical Properties of Sea-Ice Deformation Fields, Journal of Geophysical Research: Oceans, 127, https://doi.org/10.1029/2021jc017667, 2022.

445 Clauset, A., Shalizi, C. R., and Newman, M. E. J.: Power-Law Distributions in Empirical Data, SIAM Review, 51, 661–703, https://doi.org/10.1137/070710111, publisher: Society for Industrial and Applied Mathematics, 2009.

Coulomb, C.: Test on the applications of the rules of maxima and minima to some problems of statics related to architecture, Mem Math Phys, 7, 343–382, 1773.

Coulomb, C. A.: Essai sur une application des règles de maximis & minimis à quelques problèmes de statique, relatifs à l'architecture, Paris:
450 De l'Imprimerie Royale, 1776.

Cunningham, G., Kwok, R., and Banfield, J.: Ice lead orientation characteristics in the winter Beaufort Sea, in: Proceed-
ings of IGARSS '94 - 1994 IEEE International Geoscience and Remote Sensing Symposium, vol. 3, pp. 1747–1749 vol.3, https://doi.org/10.1109/IGARSS.1994.399553, 1994.

Dansereau, V., Weiss, J., Saramito, P., and Lattes, P.: A Maxwell elasto-brittle rheology for sea ice modelling, The Cryosphere, 10, 1339–
455 1359, https://doi.org/10.5194/tc-10-1339-2016, 2016.

Drucker, D. C.: A Definition of Stable Inelastic Material, Journal of Applied Mechanics, 26, 101–106, https://doi.org/10.1115/1.4011929, 1959.

Erlingsson, B.: Two-dimensional deformation patterns in sea ice, Journal of Glaciology, 34, 301–308, 1988.

Erlingsson, B.: The propagation of characteristics in sea-ice deformation fields, Annals of Glaciology, 15, 73–80, 1991.

460 Feltham, D. L.: Granular flow in the marginal ice zone, Philosophical Transactions of the Royal Society A: Mathematical, Physical and Engineering Sciences, 363, 1677–1700, https://doi.org/10.1098/rsta.2005.1601, publisher: Royal Society, 2005.

Golding, N., Schulson, E. M., and Renshaw, C. E.: Shear faulting and localized heating in ice: The influence of confinement, Acta Materialia, 58, 5043–5056, https://doi.org/10.1016/j.actamat.2010.05.040, 2010.

Heorton, H. D. B. S., Feltham, D. L., and Tsamados, M.: Stress and deformation characteristics of sea ice in a high-resolution, anisotropic
465 sea ice model, Phil. Trans. R. Soc. A, 376, 20170 349, https://doi.org/10.1098/rsta.2017.0349, 2018.

Hibler, W. D.: A Dynamic Thermodynamic Sea Ice Model, Journal of Physical Oceanography, 9, 815–846, https://doi.org/10.1175/1520-0485(1979)009<0815:ADTSIM>2.0.CO;2, 1979.

Hollands, T. and Dierking, W.: Performance of a multiscale correlation algorithm for the estimation of sea-ice drift from SAR images: initial results, Annals of Glaciology, 52, 311–317, https://doi.org/10.3189/172756411795931462, 2011a.

470   Hollands, T. and Dierking, W.: Performance of a multiscale correlation algorithm for the estimation of sea-ice drift from SAR images: initial results, Annals of Glaciology, 52, 311–317, https://doi.org/10.3189/172756411795931462, publisher: Cambridge University Press, 2011b.

Hopkins, M. A.: On the ridging of intact lead ice, Journal of Geophysical Research: Oceans, 99, 16 351–16 360, https://doi.org/10.1029/94JC00996, 1994.

Hutchings, J. K., Heil, P., and Hibler, W. D.: Modeling Linear Kinematic Features in Sea Ice, Monthly Weather Review, 133, 3481–3497,

475   https://doi.org/10.1175/MWR3045.1, 2005.

Hutchings, J. K., Roberts, A., Geiger, C., and Richter-Menge, J.: Spatial and temporal characterization of sea-ice deformation, Annals of Glaciology, 52, 360–368, https://doi.org/10.3189/172756411795931769, 2011a.

Hutchings, J. K., Roberts, A., Geiger, C. A., and Richter-Menge, J.: Spatial and temporal characterization of sea-ice deformation, Annals of Glaciology, 52, 360–368, https://doi.org/10.3189/172756411795931769, 2011b.

480   Hutter, N.: lkf_tools: a code to detect and track Linear Kinematic Features (LKFs) in sea-ice deformation data (Version v1.0), https://doi.org/10.5281/zenodo.2560078, 2019.

Hutter, N.: lkf_tools: a code to detect and track Linear Kinematic Features (LKFs) in sea-ice deformation data, new version, https://doi.org/to come, 2023.

Hutter, N. and Losch, M.: Feature-based comparison of sea ice deformation in lead-permitting sea ice simulations, The Cryosphere, 14,

485   93–113, https://doi.org/10.5194/tc-14-93-2020, 2020.

Hutter, N., Martin, L., and Dimitris, M.: Scaling Properties of Arctic Sea Ice Deformation in a High-Resolution Viscous-Plastic Sea Ice Model and in Satellite Observations, Journal of Geophysical Research: Oceans, 123, 672–687, https://doi.org/10.1002/2017JC013119, 2018.

Hutter, N., Zampieri, L., and Losch, M.: Linear Kinematic Features (leads & pressure ridges) detected and tracked in RADARSAT Geophys-

490   ical Processor System (RGPS) sea-ice deformation data from 1997 to 2008, https://doi.org/10.1594/PANGAEA.898114, 2019.

Hutter, N., Zampieri, L., and Losch, M.: Leads and ridges in Arctic sea ice from RGPS data and a new tracking algorithm, The Cryosphere, 13, 627–645, https://doi.org/https://doi.org/10.5194/tc-13-627-2019, publisher: Copernicus GmbH, 2019a.

Hutter, N., Zampieri, L., and Losch, M.: Linear Kinematic Features (leads & pressure ridges) detected and tracked in RADARSAT Geophysical Processor System (RGPS) sea-ice deformation data from 1997 to 2008, https://doi.org/10.1594/PANGAEA.898114, publication

495   Title: Alfred Wegener Institute, Helmholtz Centre for Polar and Marine Research, Bremerhaven, 2019b.

Hutter, N., Bouchat, A., Dupont, F., Dukhovskoy, D., Koldunov, N., Lee, Y. J., Lemieux, J., Lique, C., Losch, M., Maslowski, W., Myers, P. G., Ólason, E., Rampal, P., Rasmussen, T., Talandier, C., Tremblay, B., and Wang, Q.: Sea Ice Rheology Experiment (SIREx): 2. Evaluating Linear Kinematic Features in High-Resolution Sea Ice Simulations, Journal of Geophysical Research: Oceans, 127, https://doi.org/10.1029/2021jc017666, 2022a.

500   Hutter, N., Bouchat, A., Dupont, F., Dukhovskoy, D., Koldunov, N., Lee, Y. J., Lemieux, J.-F., Lique, C., Losch, M., Maslowski, W., Myers, P. G., Ólason, E., Rampal, P., Rasmussen, T., Talandier, C., Tremblay, B., and Wang, Q.: Sea Ice Rheology Experiment (SIREx): 2. Evaluating Linear Kinematic Features in High-Resolution Sea Ice Simulations, Journal of Geophysical Research: Oceans, 127, e2021JC017 666, https://doi.org/10.1029/2021JC017666, _eprint: https://onlinelibrary.wiley.com/doi/pdf/10.1029/2021JC017666, 2022b.

Ip, C. F., Hibler, W. D., and Flato, G. M.: On the effect of rheology on seasonal sea-ice simulations, Annals of Glaciology, 15, 17–25, 1991.

505   Itkin, P., Losch, M., and Gerdes, R.: Landfast ice affects the stability of the Arctic halocline: Evidence from a nu-
merical model, Journal of Geophysical Research: Oceans, 120, 2622–2635, https://doi.org/10.1002/2014JC010353, _eprint:
https://agupubs.onlinelibrary.wiley.com/doi/pdf/10.1002/2014JC010353, 2015.

Keen, A., Blockley, E., Bailey, D. A., Boldingh Debernard, J., Bushuk, M., Delhaye, S., Docquier, D., Feltham, D., Massonnet, F., O'Farrell,
S., Ponsoni, L., Rodriguez, J. M., Schroeder, D., Swart, N., Toyoda, T., Tsujino, H., Vancoppenolle, M., and Wyser, K.: An inter-

510   comparison of the mass budget of the Arctic sea ice in CMIP6 models, The Cryosphere, 15, 951–982, https://doi.org/10.5194/tc-15-
951-2021, publisher: Copernicus GmbH, 2021.

Krumpen, T., Haapala, J., Krocker, R., and Bartsch, A.: Ice radar raw data (sigma S6 ice radar) of RV POLARSTERN during cruise PS122/1,
PANGAEA [dataset], https://doi.org/10.1594/PANGAEA.929434, 2021a.

Krumpen, T., von Albedyll, L., Goessling, H. F., Hendricks, S., Juhls, B., Spreen, G., Willmes, S., Belter, H. J., Dethloff, K., Haas, C.,

515   Kaleschke, L., Katlein, C., Tian-Kunze, X., Ricker, R., Rostosky, P., Rueckert, J., Singha, S., and Sokolova, J.: The MOSAiC Drift: Ice
conditions from space and comparison with previous years, The Cryosphere Discussions, pp. 1–35, https://doi.org/10.5194/tc-2021-80,
publisher: Copernicus GmbH, 2021b.

Kwok, R.: The RADARSAT Geophysical Processor System, in: Analysis of SAR Data of the Polar Oceans, pp. 235–257, Springer Berlin
Heidelberg, https://doi.org/10.1007/978-3-642-60282-5_11, 1998.

520   Kwok, R.: Deformation of the Arctic Ocean Sea Ice Cover between November 1996 and April 1997: A Qualitative Survey, in: IUTAM
Symposium on Scaling Laws in Ice Mechanics and Ice Dynamics, edited by Dempsey, J. P. and Shen, H. H., Solid Mechanics and Its
Applications, pp. 315–322, Springer Netherlands, Dordrecht, https://doi.org/10.1007/978-94-015-9735-7, 2001.

Kwok, R., Schweiger, A., Rothrock, D. A., Pang, S., and Kottmeier, C.: Sea ice motion from satellite passive mi-
crowave imagery assessed with ERS SAR and buoy motions, Journal of Geophysical Research: Oceans, 103, 8191–8214,

525   https://doi.org/https://doi.org/10.1029/97JC03334, _eprint: https://agupubs.onlinelibrary.wiley.com/doi/pdf/10.1029/97JC03334, 1998.

Linow, S. and Dierking, W.: Object-Based Detection of Linear Kinematic Features in Sea Ice, Remote Sensing, 9,
https://doi.org/10.3390/rs9050493, 2017.

Marko, J. R. and Thomson, R. E.: Rectilinear leads and internal motions in the ice pack of the western Arctic Ocean, Journal of Geophysical
Research, 82, 979–987, https://doi.org/10.1029/JC082i006p00979, 1977.

530   Marsan, D., Stern, H., Lindsay, R., and Weiss, J.: Scale Dependence and Localization of the Deformation of Arctic Sea Ice, Phys. Rev. Lett.,
93, 178 501, https://doi.org/10.1103/PhysRevLett.93.178501, 2004a.

Marsan, D., Stern, H., Lindsay, R., and Weiss, J.: Scale Dependence and Localization of the Deformation of Arctic Sea Ice, Physical Review
Letters, 93, 178 501, https://doi.org/10.1103/PhysRevLett.93.178501, 2004b.

Maykut, G. A.: Energy exchange over young sea ice in the central Arctic, Journal of Geophysical Research: Oceans, 83, 3646–3658,

535   https://doi.org/10.1029/JC083iC07p03646, _eprint: https://agupubs.onlinelibrary.wiley.com/doi/pdf/10.1029/JC083iC07p03646, 1978.

McPhee, M. G., Kwok, R., Robins, R., and Coon, M.: Upwelling of Arctic pycnocline associated with
shear motion of sea ice, Geophysical Research Letters, 32, https://doi.org/10.1029/2004GL021819, _eprint:
https://agupubs.onlinelibrary.wiley.com/doi/pdf/10.1029/2004GL021819, 2005.

Mohammadi-Aragh, M., Losch, M., and Goessling, H. F.: Comparing Arctic Sea Ice Model Simulations to Satellite Observations by Mul-

540   tiscale Directional Analysis of Linear Kinematic Features, Monthly Weather Review, 148, 3287–3303, https://doi.org/10.1175/MWR-D-
19-0359.1, publisher: American Meteorological Society Section: Monthly Weather Review, 2020.

Nguyen, A. T., Kwok, R., and Menemenlis, D.: Source and Pathway of the Western Arctic Upper Halocline in a Data-Constrained Coupled Ocean and Sea Ice Model, Journal of Physical Oceanography, 42, 802–823, https://doi.org/10.1175/JPO-D-11-040.1, publisher: American Meteorological Society, 2012.

545 Nicolaus, M., Perovich, D. K., Spreen, G., Granskog, M. A., von Albedyll, L., Angelopoulos, M., Anhaus, P., Arndt, S., Belter, H. J., Bessonov, V., Birnbaum, G., Brauchle, J., Calmer, R., Cardellach, E., Cheng, B., Clemens-Sewall, D., Dadic, R., Damm, E., de Boer, G., Demir, O., Dethloff, K., Divine, D. V., Fong, A. A., Fons, S., Frey, M. M., Fuchs, N., Gabarró, C., Gerland, S., Goessling, H. F., Gradinger, R., Haapala, J., Haas, C., Hamilton, J., Hannula, H.-R., Hendricks, S., Herber, A., Heuzé, C., Hoppmann, M., Høyland, K. V., Huntemann, M., Hutchings, J. K., Hwang, B., Itkin, P., Jacobi, H.-W., Jaggi, M., Jutila, A., Kaleschke, L., Katlein, C., Kolabutin, N., Krampe, D.,

550 Kristensen, S. S., Krumpen, T., Kurtz, N., Lampert, A., Lange, B. A., Lei, R., Light, B., Linhardt, F., Liston, G. E., Loose, B., Macfarlane, A. R., Mahmud, M., Matero, I. O., Maus, S., Morgenstern, A., Naderpour, R., Nandan, V., Niubom, A., Oggier, M., Oppelt, N., Pätzold, F., Perron, C., Petrovsky, T., Pirazzini, R., Polashenski, C., Rabe, B., Raphael, I. A., Regnery, J., Rex, M., Ricker, R., Riemann-Campe, K., Rinke, A., Rohde, J., Salganik, E., Scharien, R. K., Schiller, M., Schneebeli, M., Semmling, M., Shimanchuk, E., Shupe, M. D., Smith, M. M., Smolyanitsky, V., Sokolov, V., Stanton, T., Stroeve, J., Thielke, L., Timofeeva, A., Tonboe, R. T., Tavri, A., Tsamados, M., Wagner,

555 D. N., Watkins, D., Webster, M., and Wendisch, M.: Overview of the MOSAiC expedition: Snow and sea ice, Elementa: Science of the Anthropocene, 10, 000 046, https://doi.org/10.1525/elementa.2021.000046, 2022a.

Nicolaus, M., Perovich, D. K., Spreen, G., Granskog, M. A., von Albedyll, L., Angelopoulos, M., Anhaus, P., Arndt, S., Belter, H. J., Bessonov, V., et al.: Overview of the MOSAiC expedition: Snow and sea ice, Elem Sci Anth, 10, 000 046, 2022b.

Oda, M. and Kazama, H.: Microstructure of shear bands and its relation to the mechanisms of dilatancy and failure of dense granular soils,

560 Géotechnique, 48, 465–481, https://doi.org/10.1680/geot.1998.48.4.465, publisher: ICE Publishing, 1998.

Oikkonen, A., Haapala, J., Lensu, M., Karvonen, J., and Itkin, P.: Small-scale sea ice deformation during N-ICE2015: From compact pack ice to marginal ice zone, Journal of Geophysical Research: Oceans, 122, 5105–5120, https://doi.org/10.1002/2016JC012387, 2017a.

Oikkonen, A., Haapala, J., Lensu, M., Karvonen, J., and Itkin, P.: Small-scale sea ice deformation during N-ICE2015: From compact pack ice to marginal ice zone, Journal of Geophysical Research: Oceans, 122, 5105–5120, https://doi.org/10.1002/2016JC012387, 2017b.

565 Overland, J. E., McNutt, S. L., Salo, S., Groves, J., and Li, S.: Arctic sea ice as a granular plastic, Journal of Geophysical Research: Oceans, 103, 21 845–21 867, https://doi.org/10.1029/98JC01263, _eprint: https://agupubs.onlinelibrary.wiley.com/doi/pdf/10.1029/98JC01263, 1998.

Pritchard, R. S.: Mathematical characteristics of sea ice dynamics models, Journal of Geophysical Research: Oceans, 93, 15 609–15 618, https://doi.org/10.1029/JC093iC12p15609, 1988.

570 Rampal, P., Weiss, J., Marsan, D., Lindsay, R., and Stern, H.: Scaling properties of sea ice deformation from buoy dispersion analysis, Journal of Geophysical Research: Oceans, 113, 1–12, https://doi.org/10.1029/2007JC004143, 2008.

Ringeisen, D., Losch, M., Tremblay, L. B., and Hutter, N.: Simulating intersection angles between conjugate faults in sea ice with different viscous–plastic rheologies, The Cryosphere, 13, 1167–1186, https://doi.org/https://doi.org/10.5194/tc-13-1167-2019, 2019.

Ringeisen, D., Tremblay, L. B., and Losch, M.: Non-normal flow rules affect fracture angles in sea ice viscous–plastic rheologies, The

575 Cryosphere, 15, 2873–2888, https://doi.org/10.5194/tc-15-2873-2021, publisher: Copernicus GmbH, 2021.

Ringeisen, D., Losch, M., and Tremblay, B.: New constitutive equations for the teardrop and parabolic lens yield curves in viscous-plastic sea ice models, Earth and Space Science Open Archive, https://doi.org/10.1002/essoar.10510575.1, publisher: Earth and Space Science Open Archive Section: Oceanography, 2022.

Roscoe, K. H.: The Influence of Strains in Soil Mechanics, Géotechnique, 20, 129–170, https://doi.org/10.1680/geot.1970.20.2.129, 1970.

580 Rothrock, D. A.: The energetics of the plastic deformation of pack ice by ridging, Journal of Geophysical Research, 80, 4514–4519, https://doi.org/10.1029/JC080i033p04514, 1975.

Rothrock, D. A. and Thorndike, A. S.: Measuring the sea ice floe size distribution, Journal of Geophysical Research: Oceans, 89, 6477–6486, https://doi.org/10.1029/JC089iC04p06477, 1984.

Schall, P. and van Hecke, M.: Shear Bands in Matter with Granularity, Annual Review of Fluid Mechanics, 42, 67–88,
585 https://doi.org/10.1146/annurev-fluid-121108-145544, _eprint: https://doi.org/10.1146/annurev-fluid-121108-145544, 2010.

Schulson, E. M.: Brittle Failure of Ice, Reviews in Mineralogy and Geochemistry, 51, 201–252, https://doi.org/10.2138/gsrmg.51.1.201, publisher: GeoScienceWorld, 2002.

Schulson, E. M., Fortt, A. L., Iliescu, D., and Renshaw, C. E.: Failure envelope of first-year Arctic sea ice: The role of friction in compressive fracture, Journal of Geophysical Research: Oceans, https://doi.org/10.1029/2005JC003235, publisher: John Wiley & Sons, Ltd, 2006.

590 Stern, H. L., Rothrock, D. A., and Kwok, R.: Open water production in Arctic sea ice: Satellite measurements and model parameterizations, Journal of Geophysical Research: Oceans, 100, 20 601–20 612, https://doi.org/10.1029/95JC02306, publisher: John Wiley & Sons, Ltd, 1995.

Stern, H. L., Schweiger, A. J., Stark, M., Zhang, J., Steele, M., and Hwang, B.: Seasonal evolution of the sea-ice floe size distribution in the Beaufort and Chukchi seas, Elementa: Science of the Anthropocene, 6, https://doi.org/10.1525/elementa.305, 2018.

595 Stroeve, J., Barrett, A., Serreze, M., and Schweiger, A.: Using records from submarine, aircraft and satellites to evaluate climate model simulations of Arctic sea ice thickness, The Cryosphere, 8, 1839–1854, https://doi.org/10.5194/tc-8-1839-2014, 2014.

Tetzlaff, A., Lüpkes, C., and Hartmann, J.: Aircraft-based observations of atmospheric boundary-layer modification over Arctic leads, Quarterly Journal of the Royal Meteorological Society, 141, 2839–2856, https://doi.org/https://doi.org/10.1002/qj.2568, _eprint: https://rmets.onlinelibrary.wiley.com/doi/pdf/10.1002/qj.2568, 2015.

600 Thomas, M., Geiger, C. A., and Kambhamettu, C.: High resolution (400 m) motion characterization of sea ice using ERS-1 SAR imagery, Cold Regions Science and Technology, 52, 207–223, https://doi.org/10.1016/j.coldregions.2007.06.006, 2008.

Thomas, M., Kambhamettu, C., and Geiger, C. A.: Motion Tracking of Discontinuous Sea Ice, IEEE Transactions on Geoscience and Remote Sensing, 49, 5064–5079, https://doi.org/10.1109/TGRS.2011.2158005, conference Name: IEEE Transactions on Geoscience and Remote Sensing, 2011.

605 Thorndike, A. S., Rothrock, D. A., Maykut, G. A., and Colony, R.: The thickness distribution of sea ice, Journal of Geophysical Research, 80, 4501–4513, https://doi.org/10.1029/JC080i033p04501, 1975.

Tremblay, L.-B. and Mysak, L. A.: Modeling Sea Ice as a Granular Material, Including the Dilatancy Effect, Journal of Physical Oceanography, 27, 2342–2360, https://doi.org/10.1175/1520-0485(1997)027<2342:MSIAAG>2.0.CO;2, 1997.

Untersteiner, N.: On the mass and heat budget of arctic sea ice, Archiv für Meteorologie, Geophysik und Bioklimatologie, Serie A, 12,
610 151–182, https://doi.org/10.1007/BF02247491, 1961.

Vermeer, P. A.: The orientation of shear bands in biaxial tests, Géotechnique, https://doi.org/10.1680/geot.1990.40.2.223, 1990.

von Albedyll, L. and Hutter, N.: High resolution sea ice drift and deformation in the Transpolar Drift during MOSAiC 2019/2020, PANGAEA, submitted.

von Albedyll, L., Haas, C., and Dierking, W.: Linking sea ice deformation to ice thickness redistribution using high-resolution satellite and
615 airborne observations, The Cryosphere Discussions, pp. 1–33, https://doi.org/https://doi.org/10.5194/tc-2020-303, publisher: Copernicus GmbH, 2020.

von Albedyll, L., Hendricks, S., Grodofzig, R., Krumpen, T., Arndt, S., Belter, H. J., Birnbaum, G., Cheng, B., Hoppmann, M., Hutchings, J., Itkin, P., Lei, R., Nicolaus, M., Ricker, R., Rohde, J., Suhrhoff, M., Timofeeva, A., Watkins, D., Webster, M., and Haas, C.: Thermodynamic and dynamic contributions to seasonal Arctic sea ice thickness distributions from airborne observations, Elementa: Science of the Anthropocene, 10, 00 074, https://doi.org/10.1525/elementa.2021.00074, 2022.

Walter, B. A. and Overland, J. E.: The response of lead patterns in the Beaufort Sea to storm-scale wind forcing, Annals of Glaciology, 17, 219–226, https://doi.org/10.3189/S0260305500012878, 1993.

Wang, K.: Observing the yield curve of compacted pack ice, Journal of Geophysical Research: Oceans, 112, C05 015, https://doi.org/10.1029/2006JC003610, 2007.

Weiss, J.: Sea Ice Deformation, in: Drift, Deformation, and Fracture of Sea Ice, SpringerBriefs in Earth Sciences, pp. 31–51, Springer Netherlands, https://doi.org/10.1007/978-94-007-6202-2_3, 2013.

Weiss, J. and Dansereau, V.: Linking scales in sea ice mechanics, Phil. Trans. R. Soc. A, 375, 20150 352, https://doi.org/10.1098/rsta.2015.0352, 2017.

Wilchinsky, A. V. and Feltham, D. L.: A continuum anisotropic model of sea-ice dynamics, Proceedings of the Royal Society of London A: Mathematical, Physical and Engineering Sciences, 460, 2105–2140, https://doi.org/10.1098/rspa.2004.1282, 2004.

Wilchinsky, A. V. and Feltham, D. L.: Modeling Coulombic failure of sea ice with leads, Journal of Geophysical Research: Oceans, 116, https://doi.org/10.1029/2011JC007071, 2011.

Wilchinsky, A. V., Feltham, D. L., and Hopkins, M. A.: Effect of shear rupture on aggregate scale formation in sea ice, Journal of Geophysical Research: Oceans, 115, C10 002, https://doi.org/10.1029/2009JC006043, 2010.

Zhang, J. and Rothrock, D. A.: Effect of sea ice rheology in numerical investigations of climate, Journal of Geophysical Research: Oceans, 110, C08 014, https://doi.org/10.1029/2004JC002599, 2005.